# Probing higher order multimers of pyruvate kinase with charge detection mass spectrometry

Elizabeth E. Pierson, David Z. Keifer, Nathan C. Contino, Martin F. Jarrold*

*Chemistry Department, Indiana University 800 E. Kirkwood Avenue, Bloomington, IN 47405, United States*

## ARTICLE INFO

## ABSTRACT

Pyruvate kinase multimers have been investigated by charge detection mass spectrometry (CDMS). In CDMS, the $m/z$ and $z$ are simultaneously measured for each ion, so the mass is determined directly. The measurements were made using a modified cone trap that incorporates an image charge detector with a cryogenically cooled preamplifier. With non-denaturing solution conditions, the tetrameric form of pyruvate kinase is observed along with aggregates of the tetramer. The time-of-flight $m/z$ spectrum shows octamers and dodecamers. However, the lack of charge state resolution prevents identification of larger multimers. Multimers up to the 40-mer are revealed by CDMS. Their intensities fall-off exponentially with size. Evidence supporting a non-specific, solution-based aggregation mechanism is presented. The relationship between the $m/z$ and mass of the multimers is consistent with the predictions of the charge residue model. Pyruvate kinase ions are held in the cone trap for up to 129 ms. With this long trapping time the root mean square deviation in the charge determination is reduced to 1.3 elementary charges.

© 2013 Elsevier B.V. All rights reserved.

## 1. Introduction

Native mass spectrometry (MS) is an emerging field which applies MS to the study of protein complexes or other noncovalent assemblies [1]. Time-of-flight (TOF)-MS is prominent in this field since the technique has no theoretical upper mass limit [2], is relatively cheap, and is fairly simple to design and operate; however, the detectors used in TOF-MS, most often multichannel plates (MCPs), exhibit decreasing detection efficiency with increasing mass-to-charge ratio ($m/z$) [3]. Electrospray ionization (ESI) is well-suited to native MS for several reasons. It helps overcome the detection efficiency limitation of ion detectors such as MCPs by producing multiply charged ions which reduces the mass-to-charge ratio of the complexes so that they fall within the mass range of the mass analyzer. When charge states are well resolved, the spacing between the peaks allows for the determination of the masses of the ions from the $m/z$ spectrum. ESI is also a soft ionization technique which is capable of preserving large, noncovalent complexes in the gas phase [4–7]. ESI-TOF-MS has successfully been used to correlate the electrophoretic mobility diameter to molecular mass for large protein complexes [8], probe the structure of entire virus capsids [9], elucidate the mechanism of mismatched DNA repair [10], and investigate the effects of small stabilizing molecules on the gas-phase structure of protein complexes [11].

ESI does not resolve all of the limitations of TOF in native MS, however. Inherent mass heterogeneity as well as factors such as salt adduction and incomplete solvent evaporation lead to peak broadening. As the sizes of complexes increase, these factors become more significant, eventually leading to the loss of charge state resolution in the $m/z$ spectrum, which precludes mass deduction. Moreover, the charge state envelopes of several species may overlap, further convoluting the $m/z$ spectrum and inhibiting mass determination.

Charge detection mass spectrometry (CDMS) circumvents the need for charge state resolution in the $m/z$ spectrum by measuring both the $m/z$ and the charge of an individual ion simultaneously, providing a direct determination of the mass [12–18]. To measure the charge, the ion is passed through a conducting cylinder, impressing an image charge on the cylinder that can be detected with a charge sensitive preamplifier. The difficulty of this approach lies in the low signal-to-noise ratio associated with detecting the charge on a single ion. The noise floor is not easily forced below about 100 elementary charges (e). Signal averaging using a linear array of charge detectors [19–21] or a recirculating ion trap [22,23] can improve both the limit of detection and the precision of the charge measurement. We recently described a CDMS instrument where a dual hemispherical deflection analyzer (HDA) is coupled to a modified cone trap, leading to extended trapping times which decreased the limit of detection and improved the precision of the charge measurement [24]. Further improvement was obtained by cryogenically cooling the JFET at the input of the charge sensitive preamplifier which detects the image charge [25]. With cooling we

were able to detect single macroions with less than 10 elementary charges.

Here, CDMS has been used to collect $m/z$ and mass spectra of pyruvate kinase, an enzyme which produces pyruvate and ATP during glycolysis. Pyruvate kinase monomer is known to associate into tetramers in solution; tetramers have been observed by MS to aggregate further into octamers and dodecamers [26]. To our knowledge, there is no evidence in the literature of further aggregation of pyruvate kinase. By optimizing the interface of our mass spectrometer to transmit high $m/z$ ions, we have generated $m/z$ spectra which suggest the presence of larger aggregates of pyruvate kinase. At the high end of the spectra, the $m/z$ envelopes of different-sized aggregates overlap and peaks in the $m/z$ spectra are not sufficiently resolved to make assignments. The mass spectrum produced via CDMS, however, evinces the existence of aggregates of pyruvate kinase up to the 40-mer.

## 2. Experimental methods

The experimental apparatus used for these studies has been described in detail elsewhere [24], though some modifications have been made to the ionization source and the atmosphere-to-vacuum interface. Briefly, ions are generated using a nano-electrospray source (Advion Biosciences, Ithaca, NY, USA). They are transferred into vacuum through a 10 cm long stainless steel capillary (0.75 mm ID) heated to 100 °C. The ions are then focused and transported through three consecutive differentially pumped regions containing an ion funnel, hexapole, and quadrupole, respectively. A DC offset on the hexapole sets the ion's nominal kinetic energy (around 100 eV/charge).

The fourth differentially pumped region contains an orthogonal TOF-MS as well as a modified cone trap [27] containing the charge detection tube. The TOF-MS is based on the design of Dodonov et al. [28]. Ions are analyzed by the TOF-MS if high-voltage pulses are applied to electrodes in the extraction region.

When the TOF extraction electrodes are held at ground potential, the ion beam passes through the extraction region to the entrance of a dual hemispherical deflection analyzer (HDA) that selects a band of kinetic energies. In some of the experiments described here, the dual HDA was operated in a high resolution mode where the ions are decelerated to 10 eV/charge before transmission through the dual HDA and then accelerated to 100 eV/charge upon exiting. In the high resolution mode the energy spread of the transmitted ion beam is around 0.6 eV/charge FWHM [25]. The rest of the experiments were performed in a low resolution mode where the ions are not decelerated before passage through the dual HDA. In this mode, the energy spread of the ion beam exiting the dual HDA is approximately 3.3 eV/charge FWHM. Ions transmitted through the dual HDA pass into the modified cone trap where some of them are trapped for charge detection measurements.

At the beginning of the trapping cycle the voltages on the front and back end caps of the trap are set to 0 V, and ions pass through the trap unimpeded. After around 1 ms, the trapping voltage (135 V) is applied to the back end cap and shortly after, the same voltage is applied to the front end cap. Ions with a nominal kinetic energy of 100 eV/charge are trapped and cycle back and forth through the charge detection tube at the center of the trap. The ions are trapped for up to 129 ms; then the voltages on the front and back end caps are returned to 0 V, and the trapping cycle begins again.

As an ion passes through the charge detection tube an image charge is induced that is detected by a JFET (2SK152) at the input of a charge-sensitive preamplifier (Amptek A250). The JFET is cooled to ~125 K by means of liquid nitrogen reservoir housed in the vacuum chamber. The periodic signal due to an ion recycling back and forth within the trap is extracted from the raw data with a fast Fourier
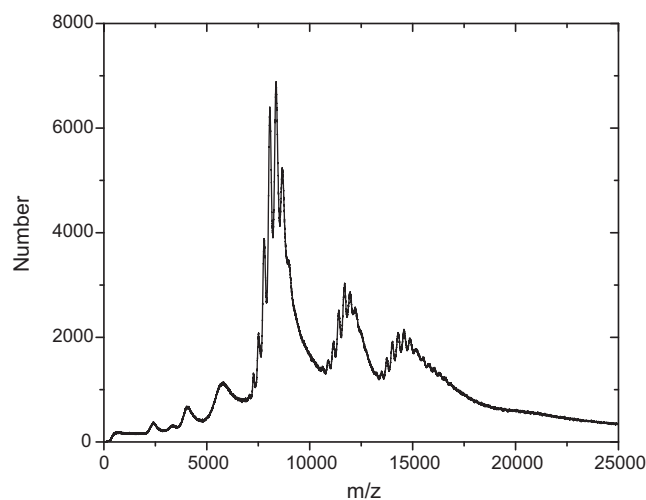


**Fig. 1.** $m/z$ spectrum measured for pyruvate kinase by TOF mass spectrometry.

transform (FFT). The FFT contains the fundamental frequency of the ion as well as harmonics. The data analysis program identifies the fundamental frequency, $f$, and uses it to calculate the $m/z$ of the ion using [24]:

$$\frac{m}{z} = \frac{C}{E_0 f^2} \qquad (1)$$

where $E_0$ is the nominal ion energy and $C$ is a calibration constant that is deduced empirically from Simion simulations.

Pyruvate kinase from rabbit muscle was purchased from Sigma–Aldrich (St Louis, MO, USA). The protein was prepared at a concentration of 23 μM in 100 mM ammonium acetate and purified via size-exclusion chromatography. Under the non-denaturing solution conditions used here, pyruvate kinase exists primarily as a tetramer [29].

## 3. Results

Fig. 1 shows the $m/z$ spectrum measured for pyruvate kinase using the TOF mass spectrometer. In these experiments, a constant bin width of 3.2 ns was used. Use of shorter bins was investigated, but resolution was not improved. The largest charge state envelope, centered around $m/z$ = 8000 Th, is due to the pyruvate kinase tetramer $PK_4$. The smaller charge state envelopes centered around $m/z$ = 11,000 Th and 13,500 Th are due to the octamer $(PK_4)_2$ and dodecamer $(PK_4)_3$, respectively. Ions are present at higher $m/z$ (>15,000 Th), but the lack of charge state resolution prevents their identification. The signals below 6000 Th in Fig. 1 are not readily identifiable because of the lack of charge state resolution, but they are thought to be due to residual impurities in the sample.

Fig. 2 shows the $m/z$ histogram determined for pyruvate kinase by CDMS. As noted above, the $m/z$ for each individual ion is calculated from the fundamental frequency determined by the data analysis program using a fast Fourier transform. The resulting $m/z$ values are then binned to give the histogram. Ions trapped for less than 200 cycles are excluded from all CDMS plots. This cycle cutoff is implemented because ions trapped for less than 200 cycles do not give reliable charge measurements. The results shown in Fig. 2 were recorded in the high resolution mode which provides better $m/z$ resolution. We do not show features below 5000 Th in the $m/z$ histogram to avoid the distraction of an artifact that is the result of the program used to analyze the data occasionally reporting the second harmonic as the fundamental frequency.

The features present in the CDMS $m/z$ histogram are similar to those present in the TOF $m/z$ spectrum. Features at around
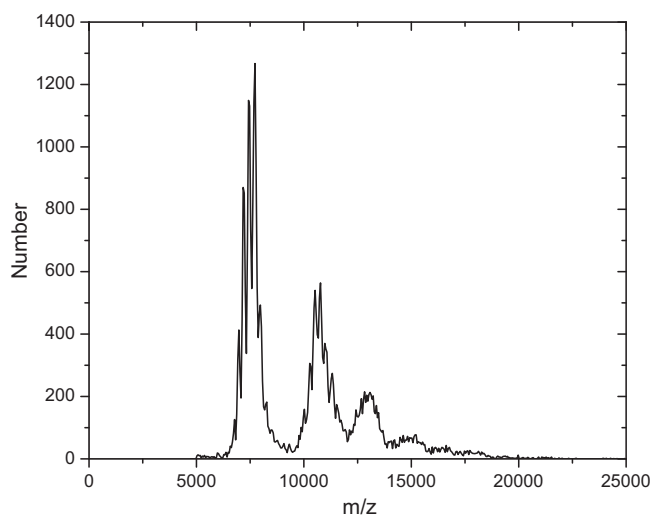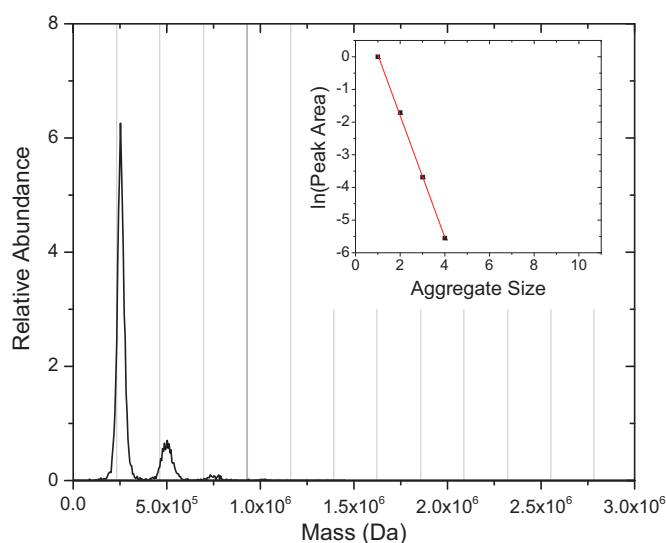
**Fig. 2.** $m/z$ histogram measured for pyruvate kinase using CDMS. The bin width is 50 Th. Features below 5000 Th are not shown because there is an artifact in this region of the spectrum (see text).

7500 Th, 11,000 Th, and 13,000 Th are due to the tetramer $PK_4$, octamer $(PK_4)_2$, and dodecamer $(PK_4)_3$. Note that these features occur at slightly different $m/z$ values in the TOF spectra and CDMS histogram. We attribute these differences to small errors in the calibration of the $m/z$ scales in both experiments. In our previous work with cytochrome c (which had well-resolved peaks in the $m/z$ histogram) we found that the $m/z$ values determined by CDMS were a few percent too low [25]. The charge state resolution in the CDMS histogram is similar to that found in the TOF $m/z$ spectrum. It diminishes with increasing $m/z$, and there is no resolution for $m/z$ values above the dodecamer.

For each ion detected in CDMS, the mass is determined by multiplying the measured $m/z$ and $z$ values. The resulting masses are binned to give the mass histogram. For reasons which will become clear below, we do not simply sum the number of ions with masses that fall into the mass bins. Instead we sum $(m/z)^{-1/2}$ for each ion. The resulting histogram is shown in Fig. 3. The signals for the higher order multimers are shown on an expanded scale ($\times 10$) for
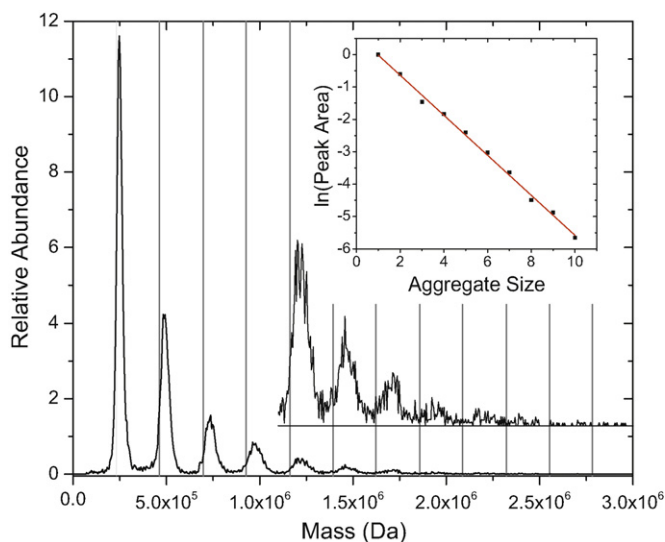


**Fig. 3.** Mass histogram measured by CDMS for pyruvate kinase with a concentration of 23 μM. The bin width is 5000 Da. The solid vertical lines show the expected positions of the multimers. The inset shows the natural log of the normalized peak areas plotted against multimer size.



**Fig. 4.** Mass histogram measured by CDMS for pyruvate kinase with a concentration of 2.3 μM. The bin width is 5000 Da. The solid vertical lines show the expected positions of the multimers. The inset shows the natural log of the normalized peak areas plotted against multimer size.

clarity. The vertical gray lines represent the expected mass of $PK_4$ and multimers of $PK_4$. Multimers up to the 40-mer $(PK_4)_{10}$ are detected. The mass histogram shows resolved peaks with average masses of 0.248, 0.492, 0.735, 0.977, 1.22, 1.47, 1.71, 1.95, 2.19, and 2.43 MDa. Each distribution is in agreement with the expected mass for multimers of $PK_4$, but the mean masses are consistently 5–6% larger than the expected values (based on a tetramer $PK_4$ mass of 232,000 Da). The inset of Fig. 3 is a plot of the natural log of the normalized peak area for each pyruvate kinase multimer as a function of multimer size. The plot is linear, indicating that the multimer abundances fall off exponentially.

Fig. 4 shows the mass histogram measured by CDMS for a pyruvate kinase solution that was diluted by a factor of 10 with 100 mM $NH_4OAc$. $PK_4$ complexes are observed along with small amounts of $(PK_4)_2$ and $(PK_4)_3$. The larger multimers that were detected with the more concentrated solution are not detected here. The inset shows the natural log of the normalized peak areas plotted against multimer size. The plot is linear with a slope that is 3.0 times steeper than the corresponding plot with the more concentrated solution.

In CDMS, the $m/z$ and mass of individual ions can be directly correlated. Fig. 5 is a scatter plot of $m/z$ versus mass where each point represents a single ion. Clusters of points represent a collection of ions that correspond to a particular multimer of pyruvate kinase. For example, the collection of points around $m/z = 7500$ Th and mass = 250,000 Da is due to the $PK_4$ tetramer, and the collection around $m/z = 10,000$ Th and mass = 500,000 Da is due to the octamer $(PK_4)_2$. The closely spaced clusters of points with $m/z$ values below 5000 Th can be ignored. They are artifacts of the data analysis program that were mentioned above.

A close inspection of Fig. 5 reveals what appear to be streaks of points on the high mass side of the large clusters of points. For example, for the cluster of points due to the pyruvate kinase tetramer at $m/z = 7500$ Th and mass = 250,000 Da, there is a streak of points that extends to around mass = 500,000 Da. For the octamer, the streak is from around 750,000 to around 1,000,000 Da, and for the dodecamer it is from around 1,000,000 to around 1,500,000 Da. We believe that the streaking is due to events where multiple ions with very similar $m/z$ values are trapped simultaneously. We keep the signal intensity low to minimize the number of multiple trapping events, and the program used to analyze the data rejects trapping events where there are signals from more than
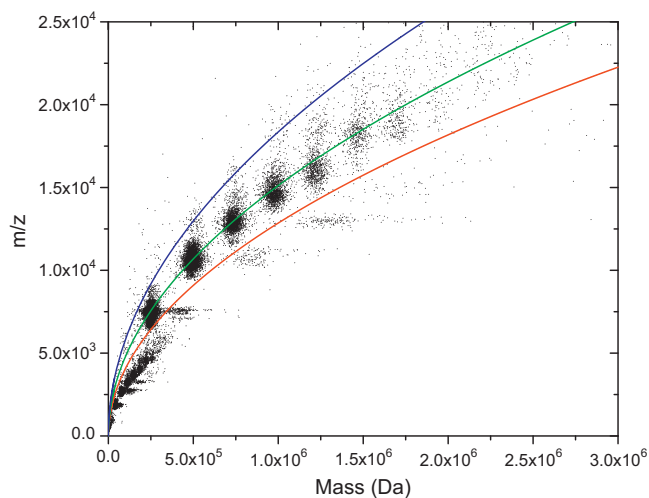
**Fig. 5.** Scatter plot of *m/z* against mass measured for pyruvate kinase with a concentration of 23 μM. Each point represents an ion. The red line shows the *m/z* values corresponding to the maximum charge (Rayleigh limit) predicted by the charge residue model. The green and blue lines show *m/z* values that correspond to charges that are 85% and 70% of the maximum charge, respectively. (For interpretation of the references to color in this figure legend, the reader is referred to the web version of this article.)



**Fig. 6.** Plot of the rms deviations of the image charge measurements against the number of cycles. The line shows the expected $n^{-1/2}$ dependence (where *n* is the number of cycles).

one ion. However, in cases where two ions with similar *m/z* values are trapped together, the FFT will detect only a single frequency. The *m/z* determination (which depends on the frequency) will be accurate, but the image charge measurement will represent the combined charge from all ions in the trap. In these cases, the data analysis program will report one ion with an appropriate *m/z* but with an artificially high charge and, consequently, an artificially high mass. When multiple ions are trapped together, they are likely to repel each other, destabilizing their trajectories and causing them to be ejected from the trap. This destabilization effect will be strongest when the charges on the ions are large. Conversely, pairs of ions with lower charge states will interact less strongly and survive in the trap for longer. So the likelihood for multiple ions to remain trapped for at least 200 cycles increases as the charges on the ions decreases. The hypothesis that these ions have a relatively low charge is supported by their locations along the mass axis. The streaks appear to cluster at masses lower than two times the mass of a single ion cluster with the same *m/z*.

In a recent paper we reported CDMS measurements for cytochrome c and ADH monomer [25]. In both cases we were able to resolve charge states in the *m/z* histogram, and by comparing the measured image charges to the charge deduced from the *m/z* distributions, we were able to determine the accuracy of the image charge measurements. We found an rms deviation of the measured image charge of 2.2 e for ions trapped for up to 29 ms. In the present work the ions are trapped for much longer, up to 129 ms. The longer trapping time should lead to a significant improvement in the accuracy of the charge measurements. As evident from Fig. 2, we also achieved charge state resolution in the *m/z* histogram of the pyruvate kinase tetramer, so we can determine the rms deviations of the image charge measurements for these ions using the procedure employed previously [25]. Fig. 6 shows the rms deviation of the measured image charge plotted against the number of cycles for the pyruvate kinase ions studied here. Results are shown for four data sets. The points at 300 cycles are the rms deviations for ions that are detected for 200–400 cycles; the points at 500 cycles are the rms deviations for ions with 400–600 cycles, and so forth. The deviations decrease from around 3.3 e for ions trapped from 200 to 400 cycles to around 1.3 e for ions trapped for 1800–2000 cycles. However, most ions do not survive for 1800–2000 cycles and the
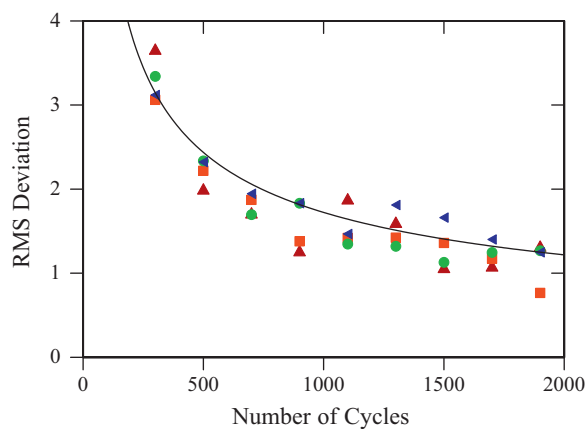
rms deviation for all ions trapped from 200 to 2000 cycles is 2.3 e. The rms deviations are expected to decline by a factor of $n^{1/2}$ where *n* is the number of cycles. The measured rms deviations roughly follow the expected behavior which is shown by the solid line in Fig. 6.

## 4. Discussion

The average masses for the pyruvate kinase multimers are 5–6% larger than expected. Some of this discrepancy could be due to an overestimate of the charge in the CDMS measurements. An overestimate was observed in prior work with cytochrome c [25]. Additionally, published TOF mass spectra of pyruvate kinase also show an overestimated mass [29] that is likely due to salt or solvent adduction. Both factors probably contribute here.

In the CDMS experiment, the density of ions in the trap before the voltages are applied to the end caps depends on the ion velocity – low velocity ions spend longer in the trap than high velocity ones, so their density is higher. For ions with the same kinetic energy/charge, the ion velocity is proportional to $(m/z)^{-1/2}$, so the density in the trap is proportional to $(m/z)^{1/2}$. Thus high *m/z* ions are more likely to be detected by CDMS than low *m/z* ions. To correct for this bias, the signals measured by CDMS should be divided by $(m/z)^{1/2}$. This correction was applied to the CDMS mass histogram (see above) so that the abundances in the mass histogram are a true reflection of the fluxes in the ion beam. However, we did not apply it to the CDMS *m/z* histogram, for reasons that will become apparent below.

A similar correction to the one outlined above should be applied to the TOF *m/z* spectrum because the ion density in the acceleration region is proportional to $(m/z)^{1/2}$. In addition, in the TOF measurement, the time required for an ion to reach the detector is proportional to $(m/z)^{1/2}$. The TOF signals are usually recorded in bins with a fixed time width so at longer times the bins contain ions from a broader range of *m/z* values than at shorter times. To account for this effect the intensities in the TOF *m/z* spectrum should be divided by another $(m/z)^{1/2}$. So overall the TOF signals should be divided by *m/z* in order to reflect the fluxes in the ion beam. However, there is another factor to consider for TOF mass spectrometry: the sensitivity of the microchannel plates used as the detector. The sensitivity is generally expected to decrease with increasing *m/z*, but it is probably a complex function of both mass and charge, and the dependences are not well characterized at present. Perhaps for this reason, TOF *m/z* spectra are not typically calibrated for these effects.
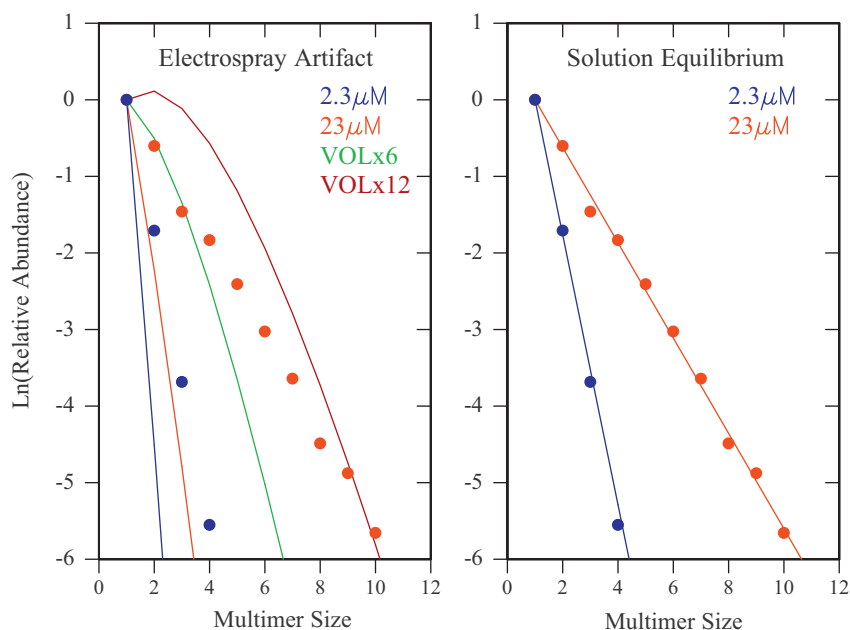
**Fig. 7.** The natural log of the relative abundances of the multimers plotted against multimer size. The red points show relative abundances measured with a solution concentration of 23 μM and the blue points were measured with a solution concentration of 2.3 μM. The solid lines show the results of simulations. In the plot on the left side the experimental results are compared to models where the multimers result from aggregation in the electrospray process (see text). In the plot on the right side the experimental results are compared to predictions of a model for solution aggregation (see text). (For interpretation of the references to color in this figure legend, the reader is referred to the web version of this article.)

The protein multimers observed here could result from aggregation in solution, or they could be an artifact of the electrospray process. It is believed that desolvated ions are generated in electrospray by two main mechanisms [30–33]. Small ions are thought to be produced mainly by an ion evaporation mechanism, where ions are field emitted from the surface of the electrospray droplet [34–36]. Large ions, like those studied here, are thought to be generated by the charge residue mechanism [30,37,38], where the solvent completely evaporates from the electrosprayed droplets, leaving behind a desolvated ion. In the charge residue mechanism, aggregates may result if more than one of the complexes present in solution is incorporated into the primary electrospray droplets.
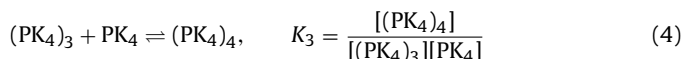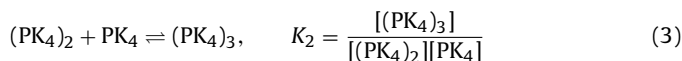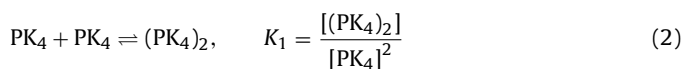
Using known scaling relationships, solution properties (conductivity and surface tension), and electrospray properties (flow rate and nozzle diameter) [39], we estimate that the primary droplets generated by electrospray under our conditions are around 50 nm in diameter. With an initial $PK_4$ concentration of 23 μM, the average probability that a droplet contains a $PK_4$ species is around 0.2. The number of $PK_4$ species in the primary droplets will follow a Poisson distribution. An electrospray operated in the cone-jet mode generates a distribution of primary droplet sizes which can be approximated by a Gaussian [40]. We average the $PK_4$ Poisson distributions (where the average probability depends on the droplet size) over a Gaussian distribution of primary droplet sizes. The results are shown in Fig. 7.

Fig. 7 shows the natural log of the multimer normalized relative abundances plotted against multimer size. The red points show the measured relative abundances for an initial concentration of 23 μM, and the blue points show them for an initial concentration of 2.3 μM. The solid red line in the plot on the left side of Fig. 7 shows the multimer abundances calculated with the Poisson distribution for an initial concentration of 23 μM, and the blue line shows the abundances calculated for an initial concentration of 2.3 μM. The multimer abundances predicted by the Poisson distribution are much smaller than observed in the experiments. The predicted change in the multimer abundances with the initial concentration is also much smaller than observed.

As a further test, we simulated an increase in the volume of the primary electrospray droplets to see if that could provide a good fit to the measured abundances. The green line in Fig. 7 shows the result of simulations where the average volume has been increased by a factor of 6 at a concentration of 23 μM. These parameters provide a good fit to the abundances of small multimers but woefully underestimate the abundances of the larger ones. With the droplet volume increased by a factor of 12 at a concentration of 23 μM (brown line in Fig. 7) the simulation comes close to predicting the correct abundances for the larger multimers but substantially overestimates the abundances of the smaller ones. In both cases, the multimer abundances fall off more rapidly than observed (a Poisson distribution falls off more rapidly than the observed exponential dependence).

In summary then, it is difficult to account for the overall abundance of the aggregates, the aggregate size distribution, and the concentration dependence in terms of an electrospray artifact, although it is possible that a small number of the aggregates may be due to this artifact.

We now explore the possibility that the aggregates result mainly from aggregation in solution through a series of coupled equilibria:

$$PK_4 + PK_4 \rightleftharpoons (PK_4)_2, \qquad K_1 = \frac{[(PK_4)_2]}{[PK_4]^2} \qquad (2)$$

$$(PK_4)_2 + PK_4 \rightleftharpoons (PK_4)_3, \qquad K_2 = \frac{[(PK_4)_3]}{[(PK_4)_2][PK_4]} \qquad (3)$$

$$(PK_4)_3 + PK_4 \rightleftharpoons (PK_4)_4, \qquad K_3 = \frac{[(PK_4)_4]}{[(PK_4)_3][PK_4]} \qquad (4)$$

etc.

As noted above, the abundances fall off roughly exponentially with increasing aggregate size. This behavior is characteristic of non-specific aggregation where the equilibrium constants $K_1$, $K_2$, $K_3$, etc. (and the corresponding free energy changes) are similar. We established a simulation for this process and then manually adjusted the equilibrium constants (with $K_1 = K_2 = K_3$, etc.) until the calculated distribution approximated the distribution measured

with an initial concentration of 23 μM. The manually optimized distribution is shown in the right panel of Fig. 7 as a solid red line. It comes close to reproducing the measured distribution. We then reduced the initial concentration by a factor of 10 and reevaluated the abundances. The result is shown in the same plot as a solid blue line. The abundances are in good agreement with those determined from the experimental results with an initial concentration of 2.3 μM. These simulations indicate that the multimers observed in the experiments are mainly due to non-specific aggregation of $PK_4$ in solution.

When proteins are electrosprayed from non-denaturing solutions (such as the 100 mM aqueous ammonium acetate used here), they are expected to retain the compact folded structure present in solution. In the charge residue mechanism mentioned above, the extent of analyte charging can then be predicted from the Rayleigh charge limit for a water droplet with the same size as the analyte [6]. Heck and van den Heuvel have derived a simplified equation relating mass and maximum protein charge, $Z_R$, assuming that the protein or protein complex is spherical and has the same density as water so that the nominal radius can be estimated from the mass of the protein [41]. That relationship can be manipulated to relate $m/z$ to mass:

$$\frac{m}{Z_R} = \frac{m^{1/2}}{0.0778} \tag{5}$$

The solid red line in Fig. 5 shows the predicted variation in $m/Z_R$ plotted against the mass. The clusters of points (corresponding to the different multimer sizes) track the predicted dependence of $m/Z_R$ with mass, but the clusters of points all lie at slightly larger $m/z$ values than predicted. This indicates that the pyruvate kinase multimers carry a charge that is slightly less than the maximum predicted by the model described above. Indeed, de la Mora [6] argued that the charge on a spherical ion generated by the charge residue mechanism should lie between 70% and 100% of the maximum value because daughter droplets generated by a Rayleigh discharging event are charged to around 70% of the Rayleigh limit while the remaining primary droplet is charged to around 85% of the Rayleigh limit. The green line in Fig. 5 shows the $m/z$ values expected if the ions were charged to 85% of the Rayleigh limit, and the blue line shows the $m/z$ values for charging to 70%. The clusters of points lie on the 85% line, and only a few points lie beyond the 70% line. The model described above is not very rigorous, so it is not appropriate to put much weight on small deviations between the results and the model predictions. However, we can certainly conclude that the results are consistent with the charge residue mechanism.

The charge residue mechanism described above predicts that the $m/z$ is proportional to $m^{1/2}$, and the experimental results (Fig. 5) show this dependence. As a consequence of this dependence, the separation between the $m/z$ envelopes of the multimers diminishes as the mass increases, and for the larger multimers the $m/z$ envelopes overlap. This is why the larger multimers were not assignable in the $m/z$ spectra (both TOF and CDMS). The overlapping $m/z$ distributions provide a fundamental limitation to traditional mass spectrometry methods that prevents the differentiation and identification of large proteins and noncovalently bound complexes, particularly when the sample is not pure, or there is a mixture of several complexes. Conversely, this clearly illustrates the utility of CDMS measurements, where resolution is not lost along the mass axis because the spacing between complexes depends only on their difference in mass.

Mass spectrometry of large complexes is characterized by significant peak broadening due to non-specific adduct formation and inherent mass heterogeneity (chemical broadening). A resolving power of 5000 has been achieved with the TOF mass spectrometer for smaller ions with well-defined masses, so the widths of the
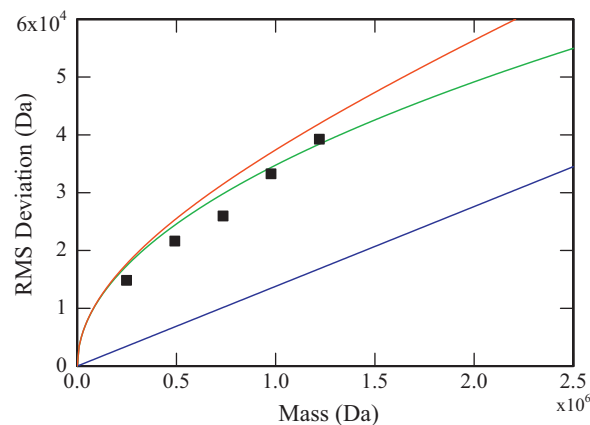


**Fig. 8.** Plots of the rms deviation against mass for the $m/z$ measurement (solid blue line), charge measurement (solid green line), and the total rms deviation (red line). The points show the rms deviations deduced from the widths of the peaks in the mass histogram (Fig. 5). (For interpretation of the references to color in this figure legend, the reader is referred to the web version of this article.)

peaks in the TOF mass spectrum of pyruvate kinase must be mainly due to the chemical broadening mentioned above.

On the other hand, the main factors contributing to the widths of the peaks in the CDMS mass histograms appear to be instrumental. There are contributions from both the $m/z$ and charge measurements. The main factors affecting the $m/z$ resolution in CDMS are the energy spread of the ion beam and the fact that the ion's oscillation frequency depends on the entry conditions (position and angle). From Eq. (1), a slightly different frequency leads to a slightly different $m/z$. The rms deviation resulting from the energy spread and the shift in the oscillation frequency is plotted as the solid blue line in Fig. 8. The rms deviation resulting from the uncertainty in the charge measurement (2.3 e) is shown by the solid green line. The overall rms deviation is given by

$$R = \sqrt{R_{m/z}^2 + R_z^2} \tag{6}$$

where $R_{m/z}$ is the rms deviation from the $m/z$ measurement and $R_z$ is the rms deviation in the charge determination. The overall rms deviation is plotted as the red line in Fig. 8. It is evident from the figure that the uncertainty in the charge determination is the main instrumental factor limiting the overall resolution. The filled points in Fig. 8 are the rms deviations obtained from the FWHM determined for the peaks in the CDMS mass histogram. We assume that the peaks are Gaussian, and then the rms deviation is the FWHM divided by 2.35482. We only show results where the signal was large enough to obtain a reliable FWHM. The points from the measurements lie slightly below the expected values shown by the red line.

## 5. Conclusions

We have used CDMS to collect $m/z$ and mass histograms for pyruvate kinase. The results reveal multimers of pyruvate kinase that cannot be detected by traditional MS methods. Our mass histogram evinces baseline-resolved peaks corresponding to multimers up to $(PK_4)_{10}$. The exponential decay in intensity of these peaks with increasing mass suggests non-specific aggregation of pyruvate kinase tetramers. By performing concentration-dependent studies and comparing the results to a model, we have concluded that this aggregation occurs primarily in solution and is not simply an artifact of the electrospray process. The relationship between the $m/z$ and mass of pyruvate kinase agrees with the charge residue model for globular protein complexes. The

measured ions have charges that are around 85% of the Rayleigh charge limit. With the long trapping time observed for some ions the rms deviation in the charge measurement was reduced to 1.3 e.

## Acknowledgements

## References

[1] A.J.R. Heck, Native mass spectrometry: a bridge between interactomics and structural biology, Nature Methods 5 (11) (2008) 927–933.
[2] M. Karas, F. Hillenkamp, Laser desorption ionization of proteins with molecular masses exceeding 10,000 Daltons, Analytical Chemistry 60 (1988) 2299–2301.
[3] I.S. Gilmore, M.P. Seah, Ion detection efficiency in SIMS: dependencies on energy, mass and composition for microchannel plates used in mass spectrometry, International Journal of Mass Spectrometry 202 (2000) 217–219.
[4] J.B. Fenn, M. Mann, C.K. Meng, S.F. Wong, C.M. Whitehouse, Electrospray ionization for mass spectrometry of large biomolecules, Science 246 (1989) 64–71.
[5] J.A. Loo, Studying noncovalent protein complexes by electrospray ionization mass spectrometry, Mass Spectrometry Reviews 16 (1) (1997) 1–23.
[6] J.F. de la Mora, Electrospray ionization of large multiply charged species proceeds via Dole's charge residue mechanism, Analytica Chimica Acta 406 (2000) 93–104.
[7] R.H. van den Heuvel, H.A.J.R. Heck, Native protein mass spectrometry: from intact oligomers to functional machineries, Current Opinion in Chemical Biology 8 (5) (2004) 519–526.
[8] C.S. Kaddis, S.H. Lomeli, S. Yin, B. Berhane, M.I. Apostol, V.A. Kickhoefer, L.H. Rome, J.A. Loo, Sizing large proteins and protein complexes by electrospray ionization mass spectrometry and ion mobility, Journal of the American Society for Mass Spectrometry 18 (2007) 1206–1216.
[9] C. Uetrecht, C. Versluis, N.R. Watts, P.T. Wingfield, A.C. Steven, A.J.R. Heck, Stability and shape of hepatitis B virus capsids in vacuo, Angewandte Chemie International Edition 47 (2008) 6247–6251.
[10] M.C. Monti, S.X. Cohen, A. Fish, H.H. Winterwerp, K. Barendregt, A. Friedhoff, P. Perrakis, A.A.J.R. Heck, T.K.R. Sixma, H. van den Heuvel, H.J.H.G. Lebbink, Native mass spectrometry provides direct evidence for DNA mismatch-induced regulation of asymmetric nucleotide binding in mismatch repair protein MutS, Nucleic Acids Research 39 (18) (2011) 8052–8064.
[11] J. Freeke, M.F. Bush, C.V. Robinson, B.T. Ruotolo, Gas-phase protein assemblies: unfolding landscapes and preserving native-like structures using noncovalent adducts, Chemical Physics Letters 524 (2012) 1–9.
[12] S.D. Fuerstenau, W.H. Benner, Molecular weight determination of megadalton DNA electrospray ions using charge detection time-of-flight mass spectrometry, Rapid Communications in Mass Spectrometry 9 (1995) 1528–1538.
[13] J.C. Schultz, C.A. Hack, W.H. Benner, Mass determination of megadatlon-DNA electrospray ions using charge detection mass spectrometry, Journal of the American Society for Mass Spectrometry 9 (1998) 305–313.
[14] J.C. Schultz, C.A. Hack, W.H. Benner, Polymerase chain reaction products analyzed by charge detection mass spectrometry, Rapid Communications in Mass Spectrometry 13 (1999) 15–20.
[15] S.D. Fuerstenau, W.H. Benner, J.J. Thomas, C. Brugidou, B. Bothner, G. Siuzdak, Mass spectrometry of an intact virus, Angewandte Chemie International Edition 40 (3) (2001) 541–544.
[16] T. Doussineau, M. Kerleroux, X.C.C. Dagany, M. Barbaire, J. Maurelli, R. Antoine, P. Dugourde, Charging megadalton poly(ethylene oxide)s by electrospray ionization. A charge detection mass spectrometry study, Rapid Communications in Mass Spectrometry 25 (2011) 617–623.

[17] T. Doussineau, C.Y. Bao, C. Clavier, X. Dagany, M. Kerleroux, R. Antoine, P. Dugourde, Infrared multiphoton dissociation tandem charge detection-mass spectrometry of single megadalton electrosprayed ions, Review of Scientific Instruments 82 (2011) 084104.
[18] T. Doussineau, C.Y. Bao, R. Antoine, P. Dugourd, W. Zhang, F. D'Agosto, B. Charleux, Direct molar mass determination of self-assembled amphiphilic block copolymer nanoobjects using electrospray-charge detection mass spectrometry, ACS Macro Letters 1 (2012) 414–417.
[19] M. Gamero-Castano, Induction charge detector with multiple sensing stages, Review of Scientific Instruments 78 (2007) 043301–043307.
[20] M. Gamero-Castano, Retarding potential and induction charge detectors in tandem for measuring the charge and mass of nanodroplets, Review of Scientific Instruments 80 (2009) 053301–053304.
[21] J.W. Smith, E.E. Siegel, J.T. Maze, M.F. Jarrold, Image charge detection mass spectrometry: pushing the envelope with sensitivity and accuracy, Analytical Chemistry 83 (2011) 950–956.
[22] W.H. Benner, A gated electrostatic ion trap to repetitiously measure the charge and *m/z* of large electrospray ions, Analytical Chemistry 69 (1997) 4162–4168.
[23] Q. Sun, L. Ding, C. Gu, Modeling and optimization of dual-cylinder image current detector in electrostatic ion beam trap for mass spectrometry, International Journal of Mass Spectrometry 282 (2009) 38–44.
[24] N.C. Contino, M.F. Jarrold, Charge detection mass spectrometry for single ions with a limit of detection of 30 charges, International Journal of Mass Spectrometry (2012), http://dx.doi.org/10.1007/s13361-012-0525-5.
[25] N.C. Contino, E.E. Pierson, D.Z. Keifer, M.F. Jarrold, Charge detection mass spectrometry with resolved charge states, Journal of Mass Spectrometry (2012), http://dx.doi.org/10.1007/s13361-012-0525-5.
[26] H. Hernandez, C.V. Robinson, Determining the stoichiometry and interactions of macromolecular assemblies from mass spectrometry, Nature Protocols 2 (3) (2007) 715–726.
[27] H.T. Schmidt, H. Cederquist, J. Jensen, A. Fardi, Conetrap: a compact electrostatic ion trap, Nuclear Instruments & Methods in Physics Research Section B 173 (2001) 523–527.
[28] A.F. Dodonov, V.I. Kozlovski, I.V. Soulimenkov, V.V. Raznikov, A.V. Loboda, Z. Zhen, T. Horwath, H. Wollnik, High-resolution electrospray ionization orthogonal time-of-flight mass spectrometry, European Journal of Mass Spectrometry 6 (2000) 481–490.
[29] J.A. Loo, Observation of large subunit protein complexes by electrospray ionization mass spectrometry, Journal of Mass Spectrometry 30 (1995) 180–183.
[30] R.B. Cole, Some tenets pertaining to electrospray ionization mass spectrometry, Journal of Mass Spectrometry 35 (2000) 763–772.
[31] P. Kebarle, Brief overview of the present status of the mechanisms involved in electrospray mass spectrometry, Journal of Mass Spectrometry 35 (2000) 804–817.
[32] P. Kebarle, M. Peschke, On the mechanism by which charged droplets produced by electrospray lead to gas phase ions, Analytica Chimica Acta 406 (2000) 11–35.
[33] N.B. Cech, C.G. Enke, Practical implications of some recent studies in electrospray ionization fundamentals, Mass Spectrometry Reviews 20 (2001) 362–387.
[34] J.V. Iribarne, B.A. Thomson, On the evaporation of small ions from charged droplets, Journal of Chemical Physics 64 (1976) 2287–2294.
[35] M. Gamero-Castaño, J. Fernandez de la Mora, Kinetics of small ion evaporation from the charge and mass of multiply charged clusters in electrosprays, Journal of Mass Spectrometry 35 (2000) 790–803.
[36] S. Nguyen, J.B. Fenn, Gas-phase ions of solute species from charged droplets of solutions, Proceedings of the National Academy of Sciences of the United States of America 104 (2007) 1111–1117.
[37] M. Dole, L.L. Mack, R.L. Hines, R.C. Mobley, L.P. Ferguson, M.B. Alice, Molecular beams of macroions, Journal of Chemical Physics 49 (1968) 2240–2249.
[38] L.L. Mack, P. Kralik, A. Rheude, M. Dole, Molecular beams of macroions II, Journal of Chemical Physics 52 (1970) 4977–4986.
[39] A.M. Gañán-Calvo, J. Dávila, A. Barrero, Current and droplet size in electrospraying of liquids., Scaling laws, Journal of Aerosol Science 28 (1997) 249–275.
[40] L. de Juan, J. Fernandez de la Mora, Charge and size distributions of electrospray drops, Journal of Colloid and Interface Science 186 (1997) 280–293.
[41] A.J.R. Heck, R.H.H. Van den Heuvel, Investigation of intact protein complexes by mass spectrometry, Mass Spectrometry Reviews 23 (2004) 368–389.